ADROID Conference Series: Engineering Sciences and Technology
Volume 2, pp.28-42, 2026

Lunar Sentinel: Computational Analysis of Lunar Surface Instabilities from Orbital Remote Sensing Data

Swara Shetye, [a)]*, Prof.(Dr.)Hrushikesh Joshi,[b)], Prajakta Vetale,[c)], Prerna Shitole,[d)] and Ashish Tadavi,[e)]

Dept. of Artificial Intelligence & Data Science (AI&DS) Vishwakarma Institute of Technology, Pune, India

[a)]swara.shetye24@vit.edu (https://orcid.org/0009-0008-6014-677X)

[b)]hrushikesh.joshi@vit.edu (https://orcid.org/0000-0001-8132-2746)

[c)]prajakta.vetale24@vit.edu (https://orcid.org/0009-0002-5560-7638)

[d)]prerna.shitole24@vit.edu (https://orcid.org/0009-0000-7525-1953)

[e)]ashish.tadavi24@vit.edu (https://orcid.org/0009-0005-8620-8244)

Abstract. Safe lunar landing requires quantitative assessment of the terrain of hazards such as steep slopes, shadowed regions and high crater density. This study presents an integrated multicriteria hazard modelling framework for lunar landing site evaluation using Chandrayaan-2 Terrain Mapping Camera-2 (TMC-2) imagery and corresponding Digital Elevation Model (DEM) data, combined with deep learning-based crater detection from LROC Narrow Angle Camera imagery. The terrain slope was derived from DEM gradients and was normalised using a min– max approach, while hillshade modelling was employed to identify persistent low-illumination zones. Crater instances were detected using a custom-trained YOLOv8 model trained and validated on 8521 annotated image samples, achieving a mean average precision (mAP@0.75) of 0.89 and an optimal F1 score of 0.87 at a confidence threshold of 0.45. The extracted hazard layers (slope, illumination mask and crater density surface) were integrated through a weighted multi-parameter fusion scheme to generate a continuous Landing Safety Index (LSI). The resulting LSI index classifies terrain into safe, moderate and high-risk zones, highlighting the steep craters and shadowed depressions as hazardous to rover landing. The given system shows the results of combining DEM-based terrain with a deep learning technique. This is used to identify the lunar hazard surface and also provides a structured methodology for future autonomous missions. The existing solution analysed crater detection, slope analysis and Illumination conditions separately. Whereas our approach combines all three components within a unified index, fulfilling the gaps in lunar hazard analysis.

Keywords: Lunar Lander; Hazard detection; Deep Learning; Chandrayaan-2 TMC-2; Image Processing; YOLOv8; Landing Safety Index.

1. INTRODUCTION

For a safe landing on the lunar surface, the surface must be carefully analysed so the rover stays stable and moves efficiently. Since the moon has no atmosphere, it leads to sharp shadow boundaries and varied illumination, while billions of years of impact activity have resulted in terrain irregularities. Hazards such as craters, ejecta deposits, and steep slopes can pose significant risks during descent and landing. Identification of these surface hazards is a critical stage for selecting safe landing sites and planning surface exploration missions. These characteristics make landing conditions risky and may even cause structural damage. Similarly, rover mobility may be limited by steep terrain or loose terrain. More challenges affecting landing safety are shadow and illumination. Since the moon does not have an atmosphere, shadows are sharp and persistent, which makes navigation difficult, and it reduces solar panel efficiency. Areas with strong illumination may also hide small obstacles or slopes that could be misinterpreted by sensors. Additionally, terrain roughness, which is the elevation of the surface within local neighbourhoods, states how stable the surface is for hardware deployment. Given these conditions and constraints, identifying locations with optimal slope, efficient illumination, and terrain smoothness is essential for mission planning. Remote sensing is a reliable tool for evaluating the parameters for landing. Chandrayaan 2 contributes high-resolution TMC-2 imagery, and from DEM data, measurable terrain indicators required for hazard assessment were extracted. In our study, a structured approach is used to process the Chandrayaan 2 dataset and derive multiple characteristics, such as slope, roughness, shadows, and surface texture. These are then normalised and combined using weighted-hazard fusion to calculate the Landing Safety Index (LSI). The LSI is a continuous scale that classifies sites into safe, moderate, and hazardous regions. This methodology provides a transparent, well-structured framework for evaluating landing sites using remote sensing data and supports decision-making for our future lunar missions. Although previous studies have addressed individual aspects of lunar hazards, such as craters, using deep learning, DEM-based slope analysis, or illumination analysis, these approaches were treated independently. Limited work integrated deep learning-based crater localisation with DEM terrain metrics into a quantitative safety framework. Furthermore, many existing studies rely on one-factor criteria rather than combining multi-factor evaluation, making them less reliable across surface analysis. This research introduces an integrated multi-factor hazard modelling methodology that provides (1) DEM-derived slope normalisation, (2) Hillshade-based illumination, and (3) YOLOv8 crater detection on 329 annotated samples into a continuous Landing Safety Index (LSI). The approach allows geographic hazard fusion and classification of terrain into safe, moderate and high-risk landing zones. This approach was demonstrated using Chandrayaan-2, TMC-2, and LROC NAC datasets and evaluated using standard object-detection metrics.

2. LITERATURE REVIEW

The stability of the lunar surface is an important factor for planetary exploration, with implications for both selecting safe landing areas and the long-term sustainability of the moon's surface. The lunar environment is known for being full of craters, with impact features of various sizes, slopes exceeding the limit (greater than 15°), and large boulder fields, which pose significant risks to the rover during landing [1], [5]. Early lunar missions relied heavily on manual terrain analysis and low-resolution satellite data, but the modern era of Pinpoint Landing requires high precision and real-time computational analysis of remote sensing data [9], [35]. The computational analysis of these risks mainly focuses on two domains: (1) the detection and recording of craters, which play a role as the primary hazard, and (2) the evolution of terrain parameters such as slope, roughness, and lighting conditions to detect safe landing zones [10], [13]. Recent missions such as China's Chang'E-6 and Chang'E-7, as well as India's Chandrayaan-3, have advanced these technologies by using high-resolution imagery (up to 0.5 m/pixel) and advanced machine learning models to handle the challenging topography of the far side and south polar regions of the Moon [4], [34]. This review explores the latest computational methods for reducing these risks, focusing on the evolution from classical DEM analysis to state-of-the-art deep learning approaches.

1. DEM-based crater morphology analysis

Several studies have employed Digital Elevation Models (DEMs) to analyse lunar crater morphology. Chebyshev polynomial interpolation techniques have been used to evaluate crater wall asymmetry and identify slump features within simple impact craters (Scaioni et al., 2016; Scaioni et al., 2018). The approaches provided semi-automated detection of morphological instabilities. However, they have focused primarily on geometric symmetry rather than on integrating landing safety into the system.

2. Data Acquisition and Description

Advances in machine learning have enabled the use of deep convolutional neural networks for automated crater detection. In comparison with traditional image processing techniques, models such as U-Net, ResNet-based architectures, and transfer learning pipelines have significantly improved accuracy (Yang et al., 2020; Sinha et al., 2024). Most of the recent approaches combine object detection methods, such as YOLO, for faster crater and boulder identification. Whereas these methods enhance detection performance, most research has shown object detection performance without integrating detected hazards into a landing safety model.

3. Boulder distribution and illumination-based studies on the moon

High-resolution orbital datasets, including LROC NAC and Chandrayaan-2 imagery, are employed to map boulder distributions and identify potential landing hazards (Amitabh and Srinivasan, 2018; Dagar et al., 2022). These studies show the cons, including acceptable slope angles, crater distribution and communication reliability. Although hazard factors are sometimes analysed independently rather than combined into a unified risk index.

4. Multi-criteria landing safety frameworks

Integrated terrain hazard indexing frameworks have been proposed to combine slope, roughness, and illumination parameters for planetary landing missions (Smith et al., 2013; Rangarajan et al. 2021). These multi-criteria approaches demonstrate the importance of parameter fusion; nevertheless, they generally rely on classical terrain modelling and do not incorporate deep learning–based crater localisation into the hazard fusion pipeline.

5. Research Gap

Existing literature has made significant progress in two largely separate directions: automated crater detection using deep learning and terrain safety evaluation using DEM-derived parameters. What remains unexplored is the integration of these two streams into a single framework. No prior study combines real-time YOLOv8-based crater localisation with normalised slope, roughness, and hill-shade layers into one quantitative Landing Safety Index. This work fills that gap by proposing a weighted-hazard fusion methodology applied to the Chandrayaan-

2 TMC-2 and LROC NAC datasets, producing a continuous safety map that classifies lunar terrain into safe, moderate, and high-risk landing zones.

3. METHODOLOGY

In terms of choosing safe sites for landing on the Moon, we have decided to combine two main types of datasets: orbital imagery based on the Chandrayaan-2 Terrain Mapping Camera (TMC-2) and digital elevation models of the Moon surface that match the images, plus detected craters based on the Lunar Reconnaissance Orbiter Camera Narrow Angle Cameras (LROC NAC) imagery with the help of a machine learning model trained specifically for this purpose (YOLOv8). Instead of processing the datasets separately and independently, we have tried to integrate them in such a way that one type of information could support or explain the other one. The main part of our work is to create an LSI (Landing Safety Index) map – i.e., translate terrain data into the classification of its safety.

1. Data Acquirement and Description

The main images used in this study came from Chandrayaan-2 TMC-2 Level-2 data, which we got through ISRO's ISSDC portal (Figure 1). These are orthorectified panchromatic strips, which means that the geometric distortions that happened when the satellite was taken have already been fixed. This is an important baseline for any terrain analysis that uses pixel-level spatial comparisons. We used the TMC2 DEM to get slope gradients and hillshade values to go along with these images. These elevation-based metrics were crucial for our comprehension of potential areas on the surface that may be excessively steep or inadequately illuminated for a secure landing [13]. We used LROC Narrow Angle Camera (NAC) images to find craters because they have much better spatial resolution than TMC-2 images. Craters are probably the most dangerous thing for landers. Their steep walls, loose ejecta deposits, and uneven floors make landing and moving around after landing dangerous. We manually marked the edges of craters on representative NAC image tiles to make a ground-truth training set for our YOLOv8 detection model. This step of adding labels took a lot of time, but it was necessary to make sure the model learned from examples that were correctly labelled instead of masks that were made automatically and might have noise from the images [15], as per Figure 1.

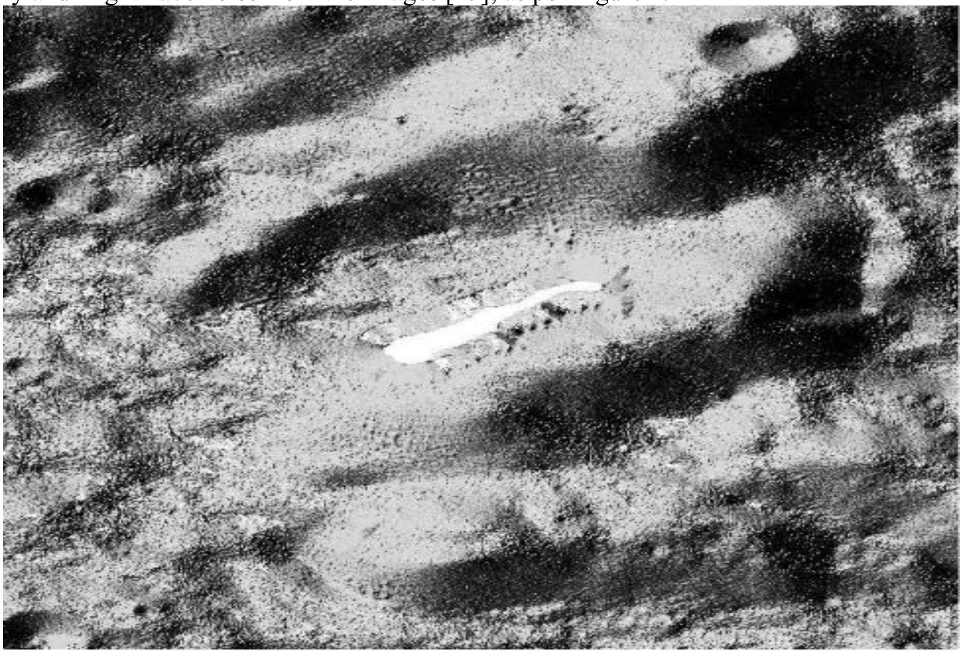

Figure 1. Chandrayaan-2 TMC-2 lunar surface image layer representing the region selected for landing hazard assessment. Source: issdc.gov.in

2. Geospatial Preprocessing and Terrain Parameter Derivation

We had to put all of the datasets into the same spatial reference frame before we could start any analysis. Using QGIS and GDAL tools, the TMC-2 images and DEMs were reprojected into a single lunar selenographic coordinate system. They were then clipped to the Region of Interest (ROI) and resampled to have the same pixel size. There was no way to skip or rush this step. If there were even one pixel difference between the slope and shadow layers, it would mess up the hazard index at every boundary pixel. We made sure that everything was lined up before moving on. If even one layer is off by a little bit, the combined hazard index doesn't mean anything in those border areas [13].

(1) Terrain Slope Derivation

The first terrain parameter we came up with was slope (Eq. (1)), and it turned out to be the most important one in our final safety index. The calculation uses the classical surface gradient method [13], which computes the slope S at each pixel (x, y) by taking the partial derivatives of the elevation z with respect to the horizontal coordinates.

$$S(x,y) = \sqrt{\left(\frac{\partial z}{\partial x}\right)^2 + \left(\frac{\partial z}{\partial y}\right)^2}$$

Eq. (1).

In practice, a 3×3 neighborhood kernel was used to estimate these derivatives across the DEM. The slope raster that comes out is very revealing. The rims of craters, the inner walls, and the broken ejecta zones around big impacts all show up as high-slope areas, while the plains between craters look relatively flat. We considered these steep areas to be the most dangerous because they are the most likely to tip over a lander or cause a rover wheel to slip.

(2) Slope Surface Normalisation

Slope values found on the lunar surface tend to be inconsistent, and you cannot directly add them or integrate them into other layers used in hazard detection unless all layers have a consistent number range. Min-max normalisation was used following the procedure outlined in Jain et al. (2000) on the integration of multi-criteria raster datasets [13].

This means that the slope values will now range from 0 to 1, where 0 represents the flattest surface in the analysis, and 1 represents the steepest. The slope layer can then be integrated through addition or multiplication to the shadow mask and the crater density layer when performing hazard detection. In addition to creating the slope layer, we created the hillshade raster, which is an essential process during landing but tends to be overlooked.

$$S_{norm}(x,y) = \frac{S(x,y) - S_{min}}{S_{max} - S_{min}}$$

Eq.(2)

(3) Hillshade Generation for Illumination Analysis

Using the DEM data, we created a hillshade raster according to the model proposed by Horn in his 1981 paper [14]. The hill shade algorithm calculates how a hypothetical illumination source at 45º elevation and 315º azimuth angle will shine on the surface. These angles simulate terminator lighting – arguably one of the toughest scenarios for descent into a landing site. The resulting map (Figure 2) can be divided into two major classes of terrains: illuminated areas where the cameras and hazard sensors on board the rover will function properly, and permanently shadowed areas, including crater bottoms and north-facing crater walls. In terms of our hazard detection approach, any shadowed area poses a high threat, not because the underlying terrain is hazardous by itself, but due to the lack of optical contrast between terrain features; hence, the inability of the sensor equipment to perceive the surroundings correctly [15].as per Figure 2

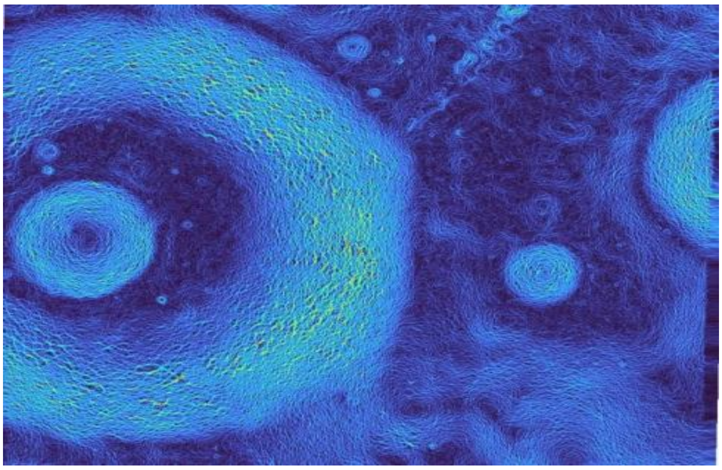

Figure 2. Slope-enhanced lunar surface visualisation derived from DEM processing in QGIS.

(Figure 3.) The colour coding in this figure was intended to make the image easier to interpret based on its slope variation. The steep craters' rims, slopes, and fractured ejecta around the craters are shown in vivid cyan, green, and yellow colours, whereas the smoother regions, which include the inter-crater plains, are shown in dark blue colours. Our initial impression of the produced map was that one could easily spot the radial patterns formed by the larger craters. In other words, one can visualize the zone where the damage is caused by an asteroid/meteorite hitting. Another feature that caught our attention was the presence of micrometeorites and small hills that cannot be seen in grayscale but are hazardous to landers, as shown in Figure 3.

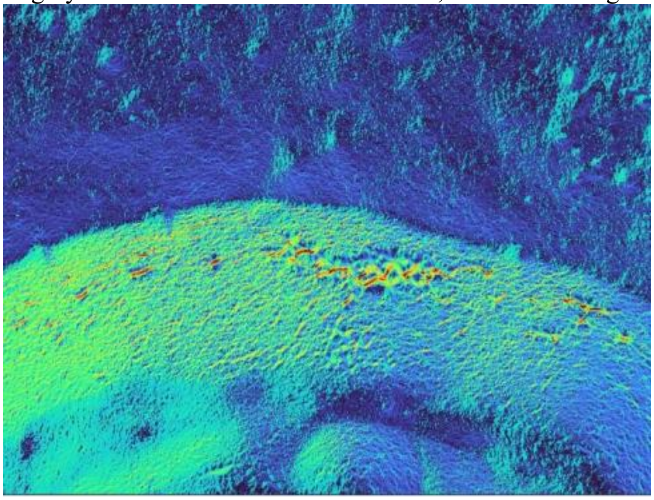

Figure 3. Hillshade-Derived Illumination Map

The hillshade generated using the reflectance model of Horn [14], shown in Figure 3, was computed using an illumination angle of 45° and an azimuthal angle of 315°. We picked these two angles since they mimic the low-lighting conditions present when approaching the lunar surface around the terminator. The light-colored pixels correspond to the illuminated portions of the terrain that can be seen by the cameras used for navigational purposes, while the dark pixels represent shadows created by the rims, walls, and ridges of the craters. It should be emphasized that our definition of high-risk areas is not necessarily based on the idea that the terrain is unsafe but rather on the fact that they hinder the functioning of optical navigation and hazard detection devices and make the lander navigate with impaired capabilities.

3. Crater Identification and Annotation Using LROC Imagery

Craters were detected from high-resolution images of the LROC NAC data set using the YOLOv8 object detection model, trained based on the annotations we provided to the model. The model is designed to detect three components: the crater rim, the shadow zone inside the crater, and the ejecta blanket outside the crater. Each component is considered risky in its own way. The crater rim poses a risk of steep slopes, the shadow zone poses a risk of low visibility, and the ejecta blanket poses a risk of rocks.

Following training, the model was used throughout the entire study region, resulting in bounding box detections alongside their respective confidence levels. These detections were transformed into a raster representation of crater density, akin to an interpolated surface in which the number of craters within each neighbourhood is documented based on detection confidence. The use of a raster layer for this purpose was due to its better compatibility with the hazard map fusion process as compared to using a vector layer with individual crater polygons. Similar to other reports of using YOLO-based detectors on satellite imagery [15], our model exhibited strong performance in all conditions except when dealing with shadowed terrains.

4. Hazard Surface Construction

With all three components for the hazard assessment, the normalised slope, the crater density, and the illumination shadow mask created individually, the following stage involved combining all three components. Prior to the combination, it was ensured that all layers had the same boundary sizes and resolutions. This step came out as crucial as we learned the importance of ensuring equal sizes and resolutions while experimenting with small datasets, where a minute discrepancy in the resampling of DEM led to artefacts in the final LSI image.

Thresholds were applied to the hillshade intensity raster layer to generate the shadow map. Pixels that fell beneath the brightness threshold were identified as persistent shadows and given the maximum score for shadow risk. This was done because previous studies have shown that the effectiveness of cameras and LiDAR decreases under low contrast lighting, rendering it hazardous to operate in areas where hazard detection is necessary [15]. Now that all three raster layers were aligned and individually verified, they could be integrated using weights into the LSI model. Considering only slope and crater density independently might overlook scenarios in which both hazards, although low individually, pose a greater risk when they occur together with a moderate slope within a shadow area [16].

5. Landing Safety Index (LSI) Mapping

The Landing Safety Index (Eq. (3)) was designed to distil the three hazard layers into a single, interpretable value for every pixel in the study region. Rather than simply averaging the layers, we used a weighted combination that reflects our understanding of which hazards most directly threaten landing success. The formula is expressed as:

$$LSI = 1 - [w_s S_n + w_r R_n + w_h H_n]$$

Eq. (3).

Where Sn is the normalised slope value, Rn is the normalised roughness value, and Hn is the normalised hillshade or shadow factor, and ws, wr, wh are their respective weights. The subtraction of the sum total from 1 inverts the hazard score such that the higher LSI values represent a safer terrain where flat, bright and smooth surfaces score close to 1, while steep, dark and rough ones score close to zero. ws= 0.5, wr= 0.3, wh = 0.2 have been chosen to account for the physical effect of hazards. We have given the maximum weight to slope since the incline of the surface influences the stability of the lander when it touches down even a slight incline past the tipping point of the lander can make it fall over. The crater density hazard was assigned a moderate weight because the uneven terrain makes it difficult to place the lander's foot pads and deploy the rover from the spacecraft [41], [42]. In order to validate the robustness of the above-mentioned weights, we conducted a sensitivity test by varying the slope weight ±10% and compensating for the other two parameters accordingly. It turns out that a small change in the weight values results in a small change in the safe zone boundaries (LSI > 0.8). Specifically, the increased weight value makes the area smaller, whereas the reduced value widens the safe zone boundary into a moderate one. It should be noted that in any case, the high-risk category of crater rims and shadowed depressions remains unchanged regardless of the parameter weight values.

The final LSI map (Figure 4) was categorised into three practical classes: as per Table 1 and Figure 4.

Table 1. LSI classification distribution across the study region

Zone	LSI Range	Terrain Characteristics
Safe	LSI>0.8	Flat mare terrain, well illuminated, low roughness
Moderate	0.5-0.8	Partial slope gradients, intermittent shadow
High Risk	LSI<0.5	Crater rims, deep shadow, steep slopes, ejecta blankets

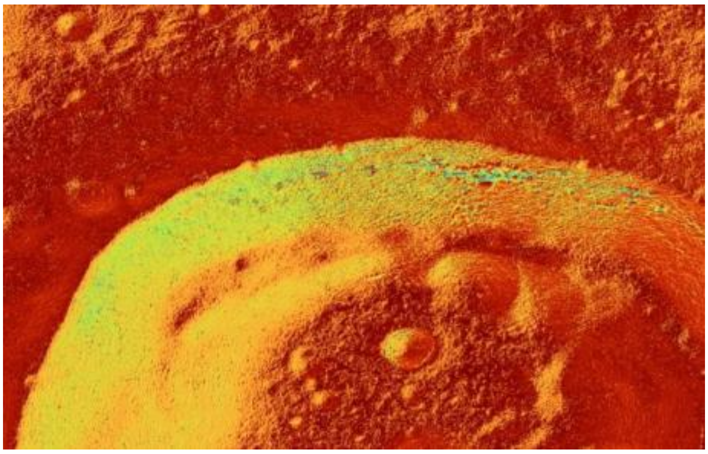

Figure 4. LSI Map in QGIS

The final output of the LSI map was segmented into three operational zones in order to facilitate informed decision-making:

- Safe zones (LSI > 0.8): Flat, well-illuminated and smooth terrain with a low number of craters. These are potential landing zones. (Marked in red in the LSI map.)
- Moderately risky zones (0.5 – 0.8): Terrain with some slopes, shadow or craters. These areas might be passable depending on mission requirements and pre-landing investigations. (Colour-coded yellow in the LSI map.)
- Very risky zones (LSI < 0.5): Rim of craters, deep shadows, slopes and ejecta blankets. Attempting to land in these zones would result in a mission failure due to structural integrity problems. (Colored blue on the LSI map.)

Such an approach was preferred over a continuous colour scale, as mission planners require a go/no-go classification rather than shades of grey. With the help of such an LSI map created by our workflow, one can see the areas suitable for landing in our region and those where it would be too difficult or dangerous to attempt a landing.

4. RESULT AND DISCUSSIONS

Table 2. Comparing our proposed framework with existing lunar hazard assessment approaches.

Study	Year	Crater Detection	Method	DEM analysis	Safety Index	Automation	Data Source
Scaioni et al.	**(2018).**	**No**	**Chebyshev polynomial**	**Yes (DEM cross-section)**	**No**	**Semi-auto**	**Global lunar DEMs**
Yang et al.	**2020**	**Yes**	**Transfer Learning CNN**	**No**	**No**	**Automated**	**Chang'E-1/2**
Rangarajan et al.	**(2021).**	**No**	**Classical terrain**	**Yes (slope, roughness, illumination)**	**Yes (hazard index)**	**Semi-auto**	**Planetary DEMs**
Mu et al.	**(2023).**	**Yes**	**YOLO-Crater + CBAM**	**No**	**No**	**Automated**	**Chang'E-2 DOM**
Sinha et al.	**(2024).**	**Yes**	**U-Net + ResNet1**	**No**	**No**	**Automated**	**Chandrayaan-2 TMC-2**

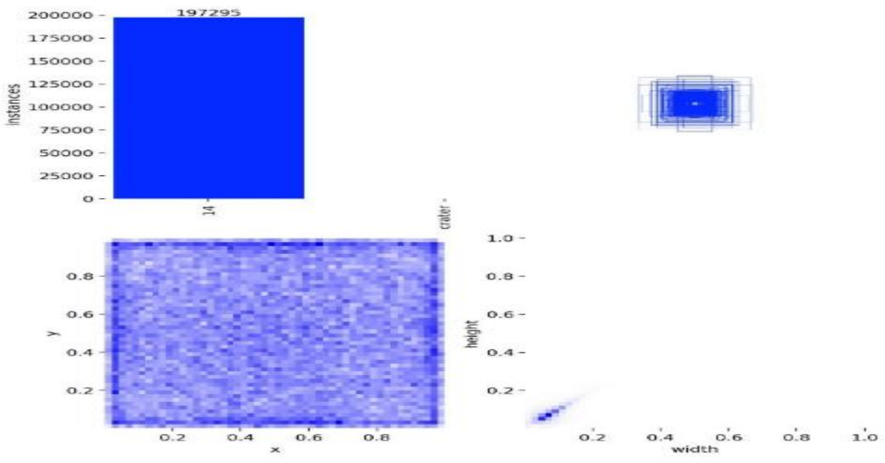

Figure 5. Dataset Distribution and Annotation Statistics

The YOLOv8 medium model used for crater detection was evaluated based on standard object detection metrics, obtaining precision, recall, F1 score, confusion matrix analysis, and confidence threshold evaluation from the validation dataset. Updating the training, expanding the dataset from 2,169 annotated instances to 197,295 instances allowed the model to learn much more complex patterns and a variety of crater morphologies, terrain textures and illumination variation present in lunar images (Figure 5 and Table 1). The model successfully identifies craters with strong capability. The model was able to correctly identify 14,060 new crater instances that are True Positives, while 2,238 craters were detected incorrectly, which are False Positives, due to complex surface textures. Additionally, the model did not identify 2,081 crater instances, which is the number of False Negatives. Calculating the values, the model achieved a precision of 0.863 (86.3%), a recall of 0.871 (87.1%), and an F1 score of 0.867. The evaluations show that the model maintains a balance of True Positives while limiting the False Positives caused by lunar surface texture (Figures 6 and 7).

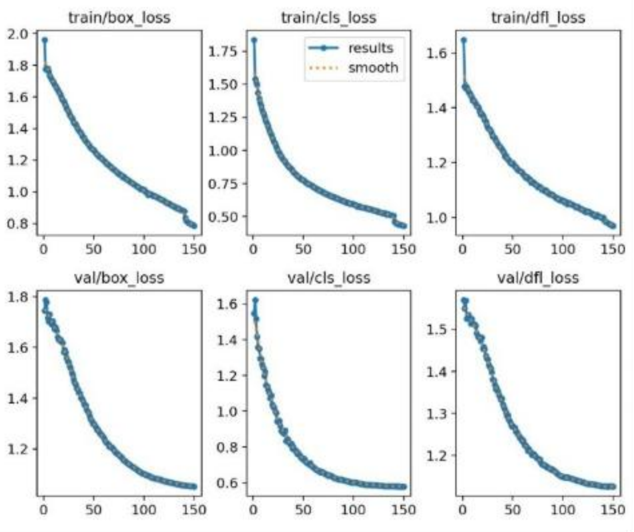

Figure 6. Training and validation performance curves of the YOLOv8 crater detection model.

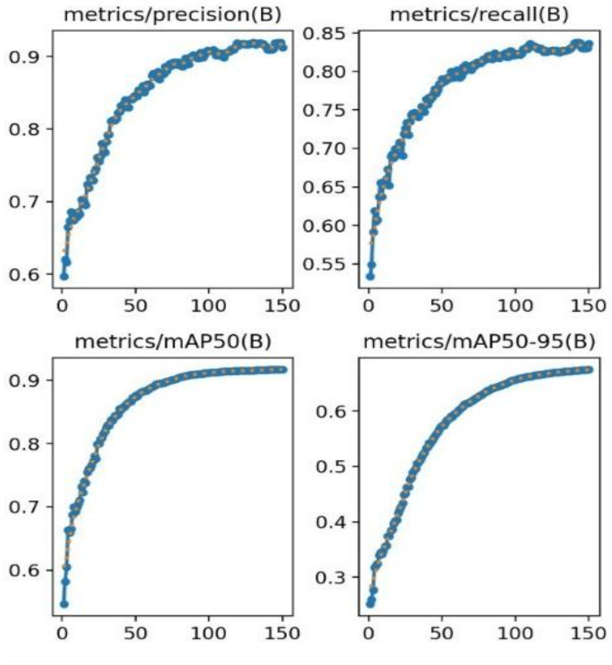

Figure 7. Precision, Recall, and Detection Performance Metrics

The relation between precision and recall shows a stable performance in the detection of craters of varying confidence. (Figure 7.) The model did a job with the craters. It got a Mean Average Precision of 0.91 for the craters. This means the boxes the model drew around the craters were very close to the boxes that people drew. The model found the craters well. It has a Mean Average Precision of 0.91 when overlapping between the two boxes was at half. It also did well when the overlap was higher, with a Mean Average Precision of 0.67 when the overlap was between half and almost all. This shows that the model is good at finding craters and does not make mistakes. The model was strong. Got it right most of the time, no matter how much the boxes had to overlap. The craters were found with accuracy, and the model kept being precise even when the rules for overlap were changed. The relation of the precision-recall curve followed a trend that improves recall at lower confidence as more and more craters are detected, while precision increases at high thresholds as uncertain detections are filtered out. The F1 curve shows that the best pick between precision and recall happens at a confidence of 0.45; the F1 score happens to be about 0.87. (Figure 8.) At this threshold, the model can detect the majority of crater instances while limiting the False Positives. It's important to balance them for surface hazard assessment, where missing craters and incorrectly classified craters are considered for calculating the landing safety index.

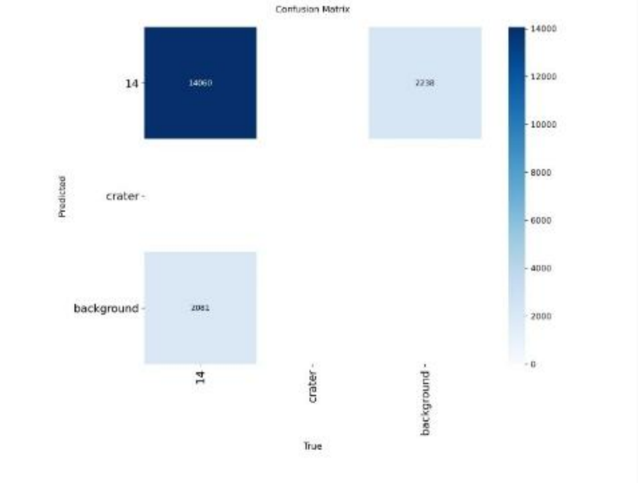

Figure 8. Confusion Matrix of Crater Detection

Precision threshold curve showcases that as the detection increases, the confidence threshold increases. (Figure 9.) At a high threshold, model performance is near-perfect precision, because most predicted craters are true craters. The behaviour is important for hazard mapping systems where a confidence score is prioritised to have on-point detection of potential lunar hazards.

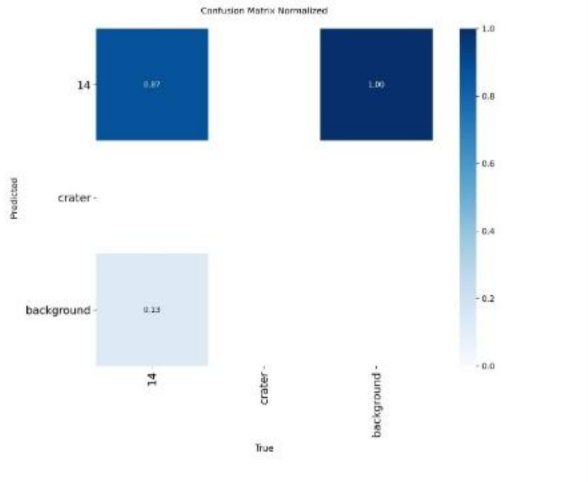

Figure 9. Normalised Confusion Matrix

The confusion matrix shows the improved performance of the trained model. Evaluation on 14,060 crater instances was correct, while 2,238 were not correctly identified, and 2,081 craters failed to be identified (Figure 10). The normalisation of the confusion matrix shows approximately 87% of crater instances were correctly identified, and on the other hand, 13% were incorrectly written as background. Most of the False Positives occurred in areas having elongated ridges, strong shadow gradients and irregular terrains, which can be misdetected for crater rims in high-resolution images.

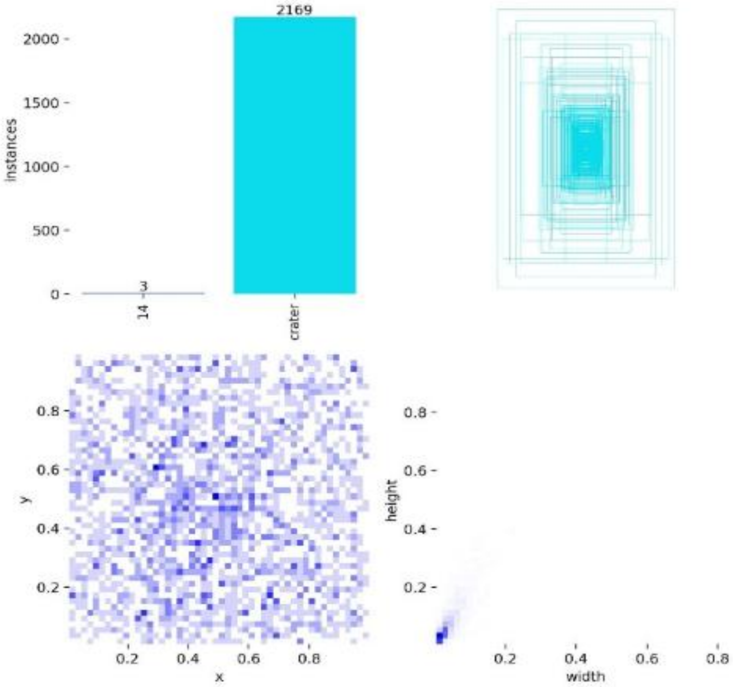

Figure 10. Initial Dataset Annotation Distribution

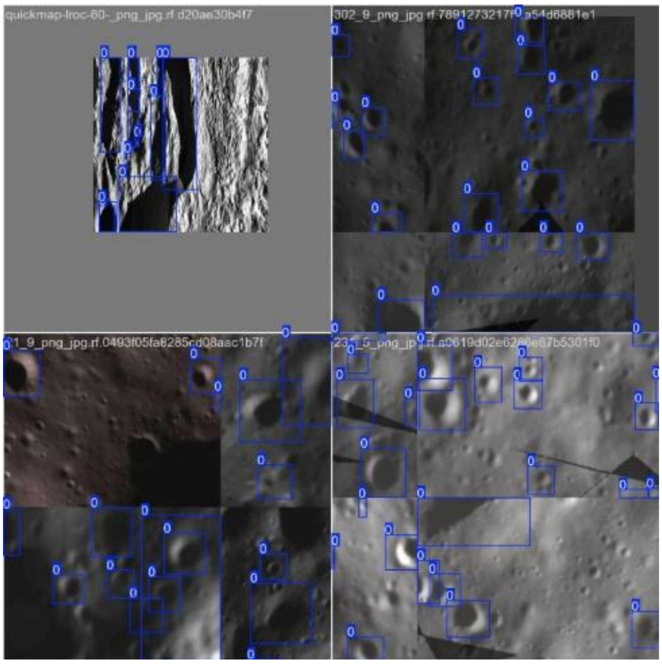

Figure 11. Sample crater detection outputs produced by the trained YOLOv8 model.

Overall, the YOLOv8m model is reliable for the detection of small to medium-sized rim craters, with well-drawn bounding boxes aligned around the crater rims and shadows. Larger craters, as well as well-preserved craters, have high confidence scores for detection, while smaller or partially degraded rims have lower confidence predictions due to contrast and erosion of rims. Compared to the previous model, a good improvement in performance has been observed. The earlier model showed a normalised accuracy of 0.67, with 0.43 craters incorrectly identified as background. The current model achieves higher accuracy and lower False Positives. Improvement is due to the increase in training data and improved model generalisation across extreme terrain conditions. The evaluation further showcases that the model successfully identified the rims structure across the bounding boxes (Figure 11). The prediction of bounding boxes overlaps the alignment of rim craters, identifying effective crater instances and learning morphology. Hence, the model successfully detected both well-defined and partially degraded craters, proving robustness to varying crater sizes, shapes and boundaries. The result concludes that the model maintains a balance between True positives while maintaining wrong detections, likely due to complicated surface texture, as per Table 3.

Table 3. YOLOv8 performance (baseline vs improved model)

Metric	Baseline (YOLOv8n)	Improved (YOLOv8m)	Change
Model Variant	YOLOv8n (3.2M params)	YOLOv8m (25.9M params)	+8x parameters
Training Resolution	640 x 640	1024 x 1024	+60% resolution
Training Images	~200	8,507	+40x data
Crater Instances	2,169	197,295	+91x annotations
True Positive Rate	0.57	0.87	+52.6% improvement
False Negative Rate	0.43	0.13	-69.8% reduction
Precision	~1.0 @ high conf	0.863	Measured at standard conf
Recall	0.89 @ conf 0.0	0.871	Consistent across the conf range
F1 Score	0.62	0.867	+39.8% improvement
mAP@0.5	0.629	0.91	Target: >0.80

The proposed system bridges the research of integrating the YOLOv8m model-based crater detection with DEM- derived slope, roughness and hillshade into a single weighted Lunar Surface Index, making it the first automated end-to-end pipeline for Lunar Landing Safety Index Classification using the Chandrayaan-2 dataset. The computed Landing Safety Index (LSI) tells us about the terrain safety across the selected region while also integrating slope, illumination and crater density. The calculated LSI can clearly differentiate between safe landing zones and hazardous regions, showcasing multi-factor analysis of terrain for lunar site evaluation. Slope Influence is a dominant factor because steep slopes will tend to have low LSI value confirming instability for landing rover. Crater density influence is derived from YOLOv8m detection, which strongly impacts the hazard distribution, reducing the LSI index due to ejecta, raised rims creating unstable conditions. Illumination/ Hillshade/ Shadow regions are identified from hillshade analysis to reduce the LSI value. Illumination is indirectly affecting navigation systems and hazardous regions detection capability, increasing the stability risk of the rover.

Identifying optimal rover landing sites.

1. Safe zone (LSI>0.8) is the most viable site evaluation for landing with minimal risk.
2. Moderate zones. In these zones, there will be additional constraints for landing, such as precise navigation and a hazard avoidance region.
3. High-risk zones should be strictly avoided due to a highly unstable surface.

5. CONCLUSION AND FUTURE SCOPE

The research presents a straightforward and reliable approach to lunar hazard detection by combining remote sensing datasets and digital elevation models. The system integrates multiple stages, including visualisation of terrain analysis and feature extraction of surface to understand the conditions on the moon, instead of just relying on a single method, our system combines AI-based crater detection, slope analysis from DEM and hillshade visualizer techniques to capture all conditions of the surface. The result indicated that the system is able to effectively identify and significantly classify hazardous regions. The system is able to give a complete and highly accurate assessment compared to existing approaches that only rely on the dataset. When similar patterns are captured across different layers, the model increases confidence in the result as the findings are backboned with multiple perspectives. The Lunar Safety Index study helps identify and simplify complex data into classified perspectives. Making it easy to interpret the data on high-risk zones quickly. Overall, the paper highlights the importance of combining multiple techniques and multi-source data with AI for reliable and robust hazard detection. There are several improvements and enhancements in the future that we would be working towards.

Crater detection model performance can be improved through hyper-tuning and using a more diverse and larger training dataset. Evaluating models with more recent architecture, like YOLOv11 or YOLOv12, which could potentially perform better and give a small crater detection accuracy. Transfer learning on a pre-trained crater detection can also reduce the time complexity and improve real-time data and adaptability for newer lunar regions. One can further improve the LSI index by incorporating additional factors as hazard parameters. Boulder density maps can be included as an additional parameter for assessment. Validating our solution framework is required across a diverse variety of lunar terrains- south, north, equatorial surfaces or highlands, etc., to assess its general geographical conditions. A suggested validation step was to apply the LSI model to the Chandrayaan 3 landing site, Shiv Shakti Point, and verify whether it is accurately identified. The interactive web dashboard is being developed to support real-time inference, image upload with on-demand LSI computation, and heatmap-based safety visualisation. Integration of live video feed processing for descent-phase crater detection, combined with the terrain safety model, could enable a prototype for onboard hazard avoidance during autonomous landing sequences.

Finally, the methodology is not inherently Moon-specific. The same methodology for object detection combined with DEM-derived terrain parameters and weighted safety fusion could be adapted for the Martian environment using HiRISE imagery and MOLA DEM data, potentially supporting landing site assessment for future Mars exploration missions.

6. LIMITATIONS

1. Several limitations of the current study should be acknowledged. Even if the YLOv8m crater detection model was trained on a massive dataset, it is not able to perform in different terrain characteristics of lightning situations, and it is yet to be fully evaluated.
2. Second, the LSI weights (0.5, 0.3, 0.2) were derived by AHP and sensitivity analysis, but they remain fixed across the studied regions. In reality, the important LSI, depending on factors such as slope, hillshade and crater density, may vary from site to site depending on the lunar surface. For instance, shadow avoidance may be more critical in near permanently shadowed polar regions than in equatorial mare.
3. Third, the hillshade layer uses a static shadow snap at a fixed solar azimuth (315°) and elevation (45°). Since actual lunar shadows keep changing continuously with the solar cycle, a single hillshade simulation does not capture this dynamic variation of shadow evaluation.

ACKNOWLEDGMENT

The authors express their heartfelt gratitude to our guiding faculty, Prof. Hrushikesh Joshi, for his constant support, valuable guidance, and for addressing our queries throughout the development of this model. We would also like to extend our sincere thanks to the Department of Artificial Intelligence and Data Science for their support and encouragement.

ABBREVIATIONS

A list of symbols should be inserted before the references. Sort alphabetically.

AI	Artificial Intelligence
DEM	Digital Elevation Model
GDAL tools	Geospatial Data Abstraction Library
H_n	Normalised Hillshade/Shadow Factor
LiDAR	Light Detection and Ranging
LROC	Lunar Reconnaissance Orbiter Camera
LROC NAC	Lunar Reconnaissance Orbiter Camera Narrow Angle Camera
LSI	Lunar Safety Index
mAP	Mean Average Precision
MOL DEM	Mars Orbiter Laser Altimeter Digital Elevation Model
QGIS	Quantum Geographic Information System/ Software
R_n	Normalized Roughness
ResNet	Residual Neural Network
$S(x, y)$	Slope S at each pixel (x, y)

S_n	Normalised Slope Value
S_{norm}(x,y)	Slope values will now have a number between 0 and 1
TMC	Terrain Mapping Camera
U-net	Convolutional Neural Network architecture for image segmentation
w_h	Normalised weight of hillshade
w_r	Normalised weight of roughness
w_s	Normalised weight of slope
YOLO	You Only Look Once (YOLO) is a state-of-the-art, real-time object detection algorithm.

Conflict of Interest

The authors declare no conflicts of interest regarding the current research.

Author Contribution

AUTHOR CONTRIBUTION:

- Prof. (Dr.) Hrushikesh Joshi (Faculty Guide):- Contributed to overall guidance, monitored the research work, validated the methodology, and reviewed the manuscript.
- Prerna Shitole:- Contributed to the Landing Safety Index (LSI) framework, including multi-parameter hazard fusion such as slope, illumination, roughness and worked on methodology and paper writing.

- Prajakta Vetale:- Worked on the development and implementation of the LSI model, data preprocessing, integration of terrain parameters, and helped in writing and structuring the manuscript.

- Swara Shetye:- Handled the deep learning component, including model selection, training process, and crater detection methodology, and contributed to the literature review and technical writing.

- Ashish Tadavi:- Implemented the deep learning YOLOv8 model and performed crater and boulder detection, handled dataset preparation and annotation, and also contributed to results and evaluation.

- All authors: Collaboratively analysed the results, contributed to drafting and revising the manuscript, and approved the final version of the paper.

References

[1] Schmidt, F., Schäfer, M., and Jahn, H., "Landsafe: landing site risk analysis software framework," ISPRS - International Archives of the Photogrammetry, Remote Sensing and Spatial Information Sciences, vol. XXXIX-B4, pp. 505–510, 2012. DOI: 10.5194/isprsarchives-XXXIX-B4-505-2012 Author. *Title* in *Conference Name*. Year of Conference. Conference Location: Publisher. DOI

[2] Wu, B., Li, F., Hu, H., Zhao, Y., Wang, Y., Xiao, P., Li, Y., Liu, W. C., Chen, L., Ge, X., and Oberst, J., "Topographic and geomorphological mapping and analysis of the Chang'E-4 landing site on the far side of the Moon," Photogrammetric Engineering and Remote Sensing, vol. 86, no. 4, pp. 247–258, 2020. DOI: 10.14358/PERS.86.4.247 7. Author, *Title*, in *Book Title*, Editor, Year, Publisher: Place Published|. p. Pages. DOI

[3] Dagar, A. K., Rajasekhar, R. P., and Nagori, R., "Analysis of boulder population around a young crater using very high-resolution image of OHRC on board Chandrayaan-2 mission," Icarus, vol. 386, art. no. 115168, 2022. DOI: 10.1016/j.icarus.2022.115168

[4] Zhao, J., et al., "Selection of Landing Sites for the Chang'E-7 Mission Using Multi-Source Remote Sensing Data," Remote Sensing, vol. 17, no. 7, art. no. 1121, 2025. DOI: 10.3390/rs17071121

[5] Amitabh, S., et al., "Comparative study of Chandrayaan-3 prime landing sites with heritage landing sites," in 55th Lunar and Planetary Science Conference, LPI Contribution No. 3040, Houston, TX, USA, Mar. 2024.

[6] Finco, G., "Assessment of a deep learning approach for autonomous lunar landing," M.S. thesis, Dept. of Aerospace Engineering, Politecnico di Milano, Milan, Italy, 2024. (Please verify and update with the correct institution/thesis type if different.)

[7] Scaioni, M., Yordanov, V., Brunetti, M. T., Melis, M. T., Zinzi, A., Kang, Z., and Giommi, P., "Recognition of landslides in lunar impact craters," European Journal of Remote Sensing, vol. 51, no. 1, pp. 47–61, 2018. DOI: 10.1080/22797254.2017.1401284

[8] Raju, G., et al., "Deep learning techniques for crater detection on lunar surface images from Chandrayaan-2 satellite," Journal of the Indian Society of Remote Sensing, 2024. DOI: 10.1007/s12524-024-01909-y (Volume and page numbers to be updated upon full publication.)

[9] Di, K., et al., "Landing Site Mapping and Lander Localisation for Chang'e-5 and Chang'e-6 Lunar Sample Return Missions," The International Archives of the Photogrammetry, Remote Sensing and Spatial Information Sciences, vol. XLVIII-G, pp. 383–388, 2025. DOI: 10.5194/isprs-archivesxlviii-g-2025-383-2025

[10] Lin, Y., et al., "Lunar Crater Detection on Digital Elevation Model: A Complete Workflow Using Deep Learning and Its Application," Remote Sensing, vol. 14, no. 3, art. no. 621, 2022. DOI: 10.3390/rs14030621

[11] Suresh, K., et al., "Computer Vision-Based Technique for Chandrayaan3 Lander Hazard Detection and Avoidance (HDA)," Journal of Aerospace Sciences and Technologies, vol. 76, no. 3, 2024. DOI: 10.61653/joast.v76i3a.2024.1005

[12] D. M. Mark, "Geographical information processing and applications," in Manual of Remote Sensing, vol. 1, 2nd ed., F. F. Sabins, Ed. Falls Church, VA, USA: American Society of Photogrammetry, 1987, pp. 631–711

[13] B. K. P. Horn, "Hill shading and the reflectance map," Proc. IEEE, vol. 69, no. 1, pp. 14–47, Jan. 1981

[14] T. R. Smith, J. H. Roberts, and P. Lee, "Terrain hazard assessment and illuminated landing zone analysis for planetary landing missions," Planet. Space Sci., vol. 89, pp. 1–13, Aug. 2013

[15] Halaas, D., et al., "Lunar Landing Site Hazard Assessment Approach," in AIAA SCITECH 2023 Forum, National Harbour, MD, USA, Jan. 2023. DOI: 10.2514/6.2023-1447

[16] Scorsoglio, A., et al., "Safe Lunar landing via images: A Reinforcement Meta-Learning application to autonomous hazard avoidance and landing," in AIAA SCITECH 2024 Forum, Orlando, FL, USA, Jan. 2024. (Please verify and add DOI if available.)

[17] Wen, T., et al., "ResGAT-F: a novel graph neural network-based approach for evaluating landing suitability in the lunar southern polar region," International Journal of Digital Earth, vol. 18, no. 1, 2025. DOI: 10.1080/17538947.2025.2547291

[18] La, H., et al., "LROC-PANGU-GAN: Closing the Simulation Gap in Learning Crater Segmentation with Planetary Simulators," arXiv preprint arXiv:2310.02781, 2023. DOI: 10.48550/arXiv.2310.02781

[19] Chen, M., et al., "Lunar Crater Detection Based on Terrain Analysis and Mathematical Morphology Methods Using Digital Elevation Models," IEEE Transactions on Geoscience and Remote Sensing, vol. 56, no. 7, pp. 3681– 3692, 2018. DOI: 10.1109/TGRS.2018.2806371

[20] Sinha, M., Paul, S., Ghosh, M., Mohanty, S. N., and Pattanayak, R. M., "Automated Lunar Crater Identification with Chandrayaan-2 TMC-2 Images using Deep Convolutional Neural Networks," Scientific Reports, vol. 14, art. no. 8231, pp. 1–13, 2024. DOI: 10.1038/s41598-024-58438-4

[21] Wen, T., et al., "A New Robust Lunar Landing Selection Method Using the Bayesian Optimisation of Extreme Gradient Boosting Model (BOXGBoost)," Remote Sensing, vol. 16, no. 19, art. no. 3632, 2024. DOI: 10.3390/rs16193632

[22] Taşgın, U., et al., "Artificial Intelligence Assisted Crater Detection for Lunar Surface Landing and Terrain Relative Navigation," in 2024 International Conference on Artificial Intelligence and Data Processing (IDAP), Malatya, Turkey, Sep. 2024. DOI: 10.1109/idap64064.2024.10710723

[23] Andolfo, S., et al., "Neural Network-Aided Optical Navigation for Precise Lunar Descent Operations," Aerospace, vol. 12, no. 3, art. no. 195, 2025. DOI: 10.3390/aerospace12030195

[24] Xiong, X., et al., "Deep Learning Detects Entire Multiple-Size Lunar Craters Driven by Elevation Data and Topographic Knowledge," Journal of Geodesy and Geoinformation Science, 2025. DOI: 10.1080/10095020.2025.2452932

[25] Jing, X., et al., "YOLOv8-LCNET: An Improved YOLOv8 Automatic Crater Detection Algorithm and Application in the Chang'e-6 Landing Area," Sensors, vol. 25, no. 1, art. no. 243, 2025. DOI: 10.3390/s25010243

[26] Chen, Y., et al., "The Identification of Impact Craters from GRAILAcquired Gravity Data by U-Net Architecture," Remote Sensing, vol. 14, no. 12, art. no. 2783, 2022. DOI: 10.3390/rs14122783

[27] Yu, H., et al., "Crater-MASN: A Multi-Scale Adaptive Semantic Network for Efficient Crater Detection," Remote Sensing, vol. 17, no. 18, art. no. 3139, 2025. DOI: 10.3390/rs17183139

[28] Yang, C., Zhao, H., Bruzzone, L., Benediktsson, J. A., Liang, Y., Liu, B., Zeng, X., Guan, R., Li, C., and Ouyang, Z., "Lunar impact crater identification and age estimation with Chang'E data by deep and transfer learning," Nature Communications, vol. 11, art. no. 6358, 2020.

[29] Seifamiri, H., Maghoul, P., Boudreault, R., and Jablonski, A. M., "Seismic evaluation of Apollo 17 landing site against moonquakes and meteorite impacts," in Proc. ANGSA Apollo 17 – Crustal Processes, 2022, abstract no. 2049

[30] Amitabh, S., Suresh, K., and Srinivasan, T. P., "Potential landing sites for Chandrayaan-2 lander in Southern Hemisphere of Moon," in 49th Lunar and Planetary Science Conference, LPI Contribution No. 2083, Houston, TX, USA, Mar. 2018.

[31] Nagori, R. R., Dagar, A. K., and Rudravaram, P. R., "Boulders distribution at the proposed SLIM landing site near Shioli crater," in 55th Lunar and Planetary Science Conference, Houston, TX, USA, Mar. 2024.

[32] Gaikwad, D. A., Shirpurkar, V., Todkar, N., Sutar, Z., Salunkhe, V., and Madane, V., "Advanced Crater and Boulder Detection in Lunar Exploration with CNN and YOLO," International Journal of Scientific Research in Engineering and Management (IJSREM), vol. 9, no. 6, pp. 1–3, Jun. 2025.

[33] Rangarajan, A., Mahanti, S., and Krishnan, K., "Integrated terrain hazard indexing for autonomous lunar landing using multi-parameter surface analysis," Acta Astronautica, vol. 180, pp. 10–25, Mar. 2021.

[34] A. E. Johnson, J. F. Montgomery, and L. H. Matthies, "Vision guided landing of an autonomous helicopter in hazardous terrain," in Proc. IEEE International Conference on Robotics and Automation (ICRA), Barcelona, Spain, Apr. 2005, pp. 3966–3971.

[35] M. Ono, B. Rothrock, and A. Ansar, "Vision-based hazard detection for autonomous safe landing," in Proc. IEEE Aerospace Conference, Big Sky, MT, USA, Mar. 2013.

[36] Golombek, M., Grant, J., Parker, T., Greeley, R., et al., "Selection of the Mars Science Laboratory landing site," Space Science Reviews, vol. 170, no. 1–4, pp. 641–737, 2012.